

Scattering and Interference in Epitaxial Graphene

G. M. Rutter,¹ J. N. Crain,² N. P. Guisinger,² T. Li,¹ P. N. First,^{1,*} J. A. Stroscio^{2,*}

¹School of Physics, Georgia Institute of Technology, Atlanta, GA 30332

²Center for Nanoscale Science and Technology, NIST, Gaithersburg, MD 20899

*Corresponding authors: joseph.stroscio@nist.gov, first@physics.gatech.edu

ABSTRACT

A single sheet of carbon, graphene, exhibits novel electronic properties that arise from unique quantum state symmetries, which restrict scattering of its charge carriers.

Understanding the role of defects in the transport properties of graphene is central to realizing a future electronics based on carbon. Scanning tunneling spectroscopy (STS) was used to measure quasiparticle interference patterns in epitaxial graphene grown on SiC(0001). Energy resolved maps of the local density of states reveal modulations on two different length scales reflecting both intravalley and intervalley scattering. While such scattering in graphene can be suppressed due to the symmetries of the Dirac quasiparticles, we show that when its source is atomic scale lattice defects wavefunctions of different symmetries can mix.

Built of a honeycomb of sp^2 bonded carbon atoms, graphene has a linear, neutrino-like, energy spectrum near the Fermi-energy. This results from the intersection of electron and hole cones in the graphene band structure at the Dirac energy, E_D . The linear energy dispersion and concomitant topological constraints give rise to massless Dirac quasiparticles in graphene, with energy-independent propagation speed $v_F \approx 10^6$ m/s. Unique symmetries of the graphene wavefunctions lead to surprising quantum properties, such as an anomalous integer quantum Hall effect [1,2] and weak anti-localization [3,4], that have spurred an intense scientific interest in graphene [5]. Bilayer graphene [5-7] is equally unique: quasiparticle states are chiral [6] with Berry's phase 2π for the bilayer versus π for the monolayer [6]. High carrier mobilities, chemical inertness, and the two-dimensional (2D) nature of graphene make it a promising candidate for future electronic device applications [1,2,5,8,9]. In particular, graphene grown epitaxially on SiC substrates and patterned via standard lithographic procedures has been proposed as a platform for carbon-based nanoelectronics and molecular electronics [8,9].

Epitaxial graphene was grown on the Si-terminated (0001) face of high purity semi-insulating 4H-SiC by thermal desorption of silicon at high temperatures [8,10]. This method produces an electron-doped graphene system, with the Fermi level 200 meV to 400 meV above E_D . The data we present was obtained from a region identified as bilayer graphene [11]. Scanning tunneling microscopy (STM) measurements were performed in a custom-built ultra-high vacuum low temperature instrument. The STS differential conductance, dI/dV , was measured with lock-in detection by applying a small modulation to the tunnel voltage at ≈ 500 Hz. Differential conductance maps were

obtained by recording an STS spectrum at each spatial pixel in the topographic measurement. All measurements reported here were taken at 4.3 K.

STM topographic images (Fig. 1) show the atomic structure and different types of disorder for epitaxial graphene on SiC(0001). At the atomic scale, the graphene is imaged as a triangular lattice (Fig. 1B), characteristic of imaging only one of the two graphene sublattices. Superimposed on this atomic structure is a modulation period of ≈ 2 nm caused by a reconstruction of the SiC interface beneath the graphene—a SiC "6x6" superstructure [12]. Survey images reveal two categories of defects. Type A defects, such as mounds (red arrow Fig. 1A) have an unperturbed graphene structure that is continuous across them, akin to a blanket. These are due to irregularities in the interface layer between graphene and the SiC bulk. In contrast, type B defects are atomic defects within the graphene lattice itself (Figs. 1A, C and D) and are accompanied by strong distortions in the local lattice images. These distortions are of electronic origin and are accompanied by large increases in the local density of states (LDOS) at the defect site [13,14]. Quasiparticle scattering from type B defects gives rise to spectacular patterns in the topographic images (Figs. 1, C and D) resulting from the symmetry of the graphene Bloch states [15-17].

Detailed information on scattering from both types of defects is obtained from STS maps of the differential conductance, dI/dV (Fig. 2), which is determined by the LDOS. By comparing the topographic and spectroscopic images we find that type B defects in the graphene lattice are the dominant scattering centers. Over much of the energy range studied, these atomic-scale defects have a large central density of states surrounded by a strong reduction in the LDOS that appears to pin the phase of the

scattering pattern nearby. For example, the type B defects labeled by blue arrows in Fig. 2 show a bright central spot encircled by a dark region and a bright ring (Figs. 2, B to E). In contrast, the dI/dV maps show that type A defects, over which the graphene is continuous (red arrows), have dramatically less influence on the LDOS.

Over large length scales, the dI/dV maps exhibit long-wavelength fluctuations that change with sample bias voltage (Figs. 2, B to E). As the sample voltage increases from -100 mV to +100 mV, the dominant wavelength decreases correspondingly from 9 nm to 5 nm. Fluctuations of much shorter wavelength are also present in these dI/dV maps, but they are not apparent over such a large displayed area. Figure 3 shows the short wavelength modulations in dI/dV maps taken with atomic-scale spatial resolution. The interference patterns in these maps display a local $\sqrt{3}\times\sqrt{3}$ R30° structure (Figs. 3, B to E) with respect to the graphene lattice, with a superimposed long-wavelength modulation. Both the long wavelength standing-wave modulations and the $\sqrt{3}\times\sqrt{3}$ periodicity are due to quasiparticle scattering from type B defects through wavevectors determined by the electronic structure of epitaxial graphene.

The two-dimensional constant energy contours in reciprocal space (Fig. 4A) are used to understand the scattering vectors that define the interference patterns observed in the STS maps of Figures 2 and 3 [18]. For graphene the constant energy contours near E_F cut through the electron and hole conical sheets resulting in small circles of radius κ , centered at the wavevectors \mathbf{K}_+ and \mathbf{K}_- that each locate 3 symmetry-equivalent corners of the 2D Brillouin zone. The scattering wavevectors \mathbf{q} connect different points on the constant energy contours (Fig. 4A). Two dominant families of scattering vectors, labeled \mathbf{q}_1 and \mathbf{q}_2 , give rise to the patterns observed in the spectroscopic conductance maps.

Wavevectors \mathbf{q}_1 connect points on a single constant-energy circle (intravalley scattering) and determine the observed long wavelength patterns. Wavevectors \mathbf{q}_2 connect constant-energy circles at adjacent \mathbf{K}_+ and \mathbf{K}_- points (intervalley scattering), yielding scattering wavevectors close in length to \mathbf{K}_\pm . \mathbf{K}_+ (\mathbf{K}_-) is related to the reciprocal lattice vectors \mathbf{G} by a rotation of 30° (-30°) and a length that is shorter by $1/\sqrt{3}$ in reciprocal space. This gives rise to the $\sqrt{3} \times \sqrt{3}$ $R30^\circ$ real space superstructures observed in the high resolution maps (Figs. 3, B to E). The vectors \mathbf{q}_2 will differ from the exact \mathbf{K}_\pm wavevector due to the finite size of the Fermi circle contours. The combination of different lengths contributing to \mathbf{q}_2 leads to the modulation of the $\sqrt{3} \times \sqrt{3}$ scattering patterns in Fig. 3.

To quantify the observed interference patterns and deduce the local band structure we obtain \mathbf{q} -space images of the scattering vectors (Fig. 4B) from Fourier transform power spectra of the spectroscopic dI/dV maps [19,20]. In Fig. 4B, \mathbf{q}_1 scattering appears as a bright ring centered at $\mathbf{q} = 0$. The ring is a consequence of the enhanced phase space for scattering near spanning vectors of the constant-energy circle. Circular disks appear centered at the \mathbf{K}_+ and \mathbf{K}_- points due to the distribution of \mathbf{q}_2 wavevectors. We determined ring radii for the central ring (Fig. 4C) and the \mathbf{K}_\pm point disks using angular averages to maximize the signal-to-noise ratio. Both features change radius as a function of bias voltage due to dispersion in the graphene electronic states, and for these extremal \mathbf{q} values, the scattering geometry determines $|\mathbf{q}| = 2\kappa$ or $|\mathbf{q} \pm \mathbf{K}_\pm| = 2\kappa$. The resulting κ -values vary linearly with energy (Fig. 4D) with a Fermi velocity of

$v_F = 9.7 \pm 0.6 \times 10^5$ m/s [18]. The $\kappa = 0$ energy intercept gives the Dirac energy, $E_F - E_D = 330 \pm 20$ meV. This local measurement of $E(\kappa)$ agrees well with photoemission studies of bilayer epitaxial graphene [7], and the parameters are close to those reported from transport studies on epitaxial graphene grown on SiC(000 $\bar{1}$) [9]. Similar results are found for a single monolayer of graphene (see fig. S1) [18].

In addition to states localized on defect sites, sharp conductance peaks, ≈ 5 meV in width, are found several nanometers from the nearest type B defect (Fig. 3). The peaks are clearly associated with the \mathbf{q}_2 -induced $\sqrt{3} \times \sqrt{3}$ LDOS modulation, as can be seen in the dI/dV maps (Figs. 3, B to E) and the spectral line profiles (Figs. 3, F to I). Furthermore, the data shows that these conductance peaks are spatially localized, with maximum intensity in regions of constructive interference (*i.e.* over broad maxima modulating the $\sqrt{3} \times \sqrt{3}$ pattern in Figs. 3, B to E). We attribute these conductance peaks to scattering resonances, which localize quasiparticles due to constructive interference in scattering from the random arrangement of defects found within a phase coherence length [18].

In support of these conclusions, Figures 3, F-I display sequences of dI/dV spectra taken along the red lines shown in Figs. 3, B to E (note that the red lines are in regions of maximum intensity modulation for the four different energies of the dI/dV maps in parts B through E). Each of the figures shows a very prominent \mathbf{q}_2 modulation along the vertical (distance) axis at the energy of the corresponding dI/dV map (B-E). The lower set of panels (J-M) show dI/dV spectra obtained at positions of the $\sqrt{3} \times \sqrt{3}$ maxima, in the general areas of constructive interference (*i.e.* near the red lines). Clearly, the energy-

dependent standing-wave patterns are associated with conductance peaks of different energies. Across the series of maps and spectra, resonances decrease in intensity as new ones acquire increased spectral strength; each corresponding to a particular spatial location of constructive interference in B to E. Resonances are seen in parts F/J at -31 mV, in G/K at -13 mV, straddling the Fermi energy at ± 1 mV in H/L, and at several energies above the Fermi level in parts I/M. Many more spectral peaks are observed for different spatial locations in the data set in Fig. 3, with equally narrow line widths.

Of particular interest is the influence of the observed scattering centers on the transport properties of epitaxial graphene. For perfect monolayer graphene, the lattice A-B site symmetry and the \mathbf{K}_{\pm} valley symmetry give rise to wavefunctions with distinct values of pseudospin and chirality [3,21,22]. Both quantities are tied directly to the group velocity of the quasiparticle wavefunction, and their near-conservation in the presence of weak potentials is equivalent to a suppression of backscattering. Our measurements of both \mathbf{q}_1 and \mathbf{q}_2 scattering processes show very directly that in-plane atomic defects are a dominant source of both intravalley (pseudospin-flip) and intervalley (chirality-reversal) backscattering. This may explain the observation of weak localization observed in similar samples [8,18]. We note that the related phenomenon of weak anti-localization was recently confirmed in epitaxial graphene grown by a different method on carbon-terminated SiC(000 $\bar{1}$) substrates [4], indicating a very low density of in-plane atomic scattering centers in those samples. Thus transport properties in epitaxial graphene are critically influenced by microscopic properties of the sample, determined (at least) by the substrate and growth conditions. For carbon-based electronics, this work

highlights the need for further microscopic studies that are correlated closely with macroscopic transport measurements.

Figure Captions

Figure 1. STM topographic images of defects in the bilayer epitaxial graphene sample. **(A)** Large field of view showing a variety defects. Type A defects (red arrow) are subsurface irregularities blanketed by graphene. The defect indicated by the red arrow has a height of 2 \AA . Type B defects are atomic-scale defects in the graphene lattice. Higher magnification images from the boxed regions in **(A)**: **(B)** a defect free region, and **(C)**, **(D)** complex scattering patterns around type B defects. Tunneling setpoint: $I = 100 \text{ pA}$, $V = 300 \text{ mV}$.

Figure 2. Defect scattering in bilayer epitaxial graphene. **(A)** STM topography and **(B-E)** simultaneously-acquired spectroscopic dI/dV maps. Type A defects (mounds) are labeled with red arrows and type B with blue arrows. Sample biases are: **(B)** -90 mV , **(C)** -60 mV , **(D)** -30 mV , and **(E)** 30 mV . $I = 500 \text{ pA}$, $V = 100 \text{ mV}$, $\Delta V = 1 \text{ mV}_{\text{RMS}}$.

Figure 3. Bilayer graphene topography **(A)**, and simultaneous dI/dV maps at sample bias voltages of **(B)** -31 mV , **(C)** -13 mV , **(D)** 1.0 mV , and **(E)** 21 mV . The type B scattering centers lie outside the image region (see lower left corner of **(A)**). **(F-I)** dI/dV (color scale) versus sample bias (horizontal axis) and distance (vertical axis) along corresponding red lines in **(B to E)**. The blue-white-red color scale spans the

conductance values observed in (J-M). **(J-M)** line-averaged dI/dV spectra obtained from regions marked by red lines in (B to E). The spectra are averages of nine curves acquired at positions of the $\sqrt{3} \times \sqrt{3}$ interference maxima in the region of the red lines. Peaks in the dI/dV spectra correlate with maxima in the long-wavelength modulation of the $\sqrt{3} \times \sqrt{3}$ interference pattern. Blue arrows indicate the bias (energy) position of the corresponding conductance images in (B to E). $I = 500$ pA, $V = 100$ mV, $\Delta V = 0.7$ mV_{RMS}.

Figure 4. **(A)** Schematic of the 2D Brillouin zone (blue), constant energy contours (green) at the \mathbf{K}_{\pm} points, and the two dominant classes of scattering vectors that create the interference patterns. Scattering wavevectors \mathbf{q}_1 (red) are seen to connect points on a single constant-energy circle, and \mathbf{q}_2 (red) connects points on constant-energy circles between adjacent \mathbf{K}_+ and \mathbf{K}_- points. **(B)** \mathbf{q} -space map of scattering amplitudes, obtained from the Fourier transform power spectrum of the dI/dV map in Fig. 2D. \mathbf{q}_1 scattering forms the small ring at $\mathbf{q} = \mathbf{0}$, while \mathbf{q}_2 events create the six circular disks at \mathbf{K}_{\pm} points. **(C)** Angular averages of the central \mathbf{q}_1 ring from the \mathbf{q} -space maps, at bias voltages from -100 mV to -20 mV shown in 10 mV increments. **(D)** Energy dispersion as a function of κ for bilayer graphene determined from the \mathbf{q} -space profiles in (C) and similar data. Values shown are derived from the radii of the central \mathbf{q}_1 scattering rings (red squares) and from the angled-averaged radii of the scattering disks at \mathbf{K}_+ and \mathbf{K}_- (blue triangles). Dashed line shows a linear fit to the data with a Fermi velocity of $v_F = 9.7 \pm 0.6 \times 10^5$ m/s, and an energy intercept of -330 ± 20 meV.

Similar results are found for a single monolayer of graphene (see fig. S2D) [18]. The larger error at lower energies results from reduced signal to noise as the modulation period approaches the image size.

Reference List

1. K. S. Novoselov *et al.*, Nature **438**, 197 (2005).
2. Y. B. Zhang, Y. W. Tan, H. L. Stormer, and P. Kim, Nature **438**, 201 (2005).
3. E. McCann *et al.*, Phys. Rev. Lett. **97**, 146805 (2006).
4. X. Wu *et al.*, Phys. Rev. Lett. **98**, 136801 (2007).
5. A. K. Geim and K. S. Novoselov, Nature Mat. **6**, 183 (2007).
6. E. McCann and V. I. Fal'ko, Phys. Rev. Lett. **96**, 086805 (2006).
7. T. Ohta *et al.*, Science **313**, 951 (2006).
8. C. Berger *et al.*, J. Phys. Chem. B **108**, 19912 (2004).
9. C. Berger *et al.*, Science **312**, 1191 (2006).
10. E. Rolling *et al.*, J. Phys. Chem. Sol. **67**, 2172 (2006).
11. The identification of single and bilayer graphene is made from counting the number of atomic steps from the SiC substrate layer combined with STS measurements. Layers are also differentiated by the appearance of Si adatom interface states visible on the single layer graphene [18].
12. F. Owman and P. Martensson, Surf. Sci. **369**, 126 (1996).
13. V. M. Pereira *et al.*, Phys. Rev. Lett. **96**, 36801 (2006).
14. T. O. Wehling *et al.*, Phys. Rev. B **75**, 125425 (2007).
15. H. A. Mizes and J. S. Foster, Science **244**, 559 (1989).
16. K. F. Kelly and N. J. Halas, Surf. Sci. **416**, L1085 (1998).
17. P. Ruffieux *et al.*, Phys. Rev. Lett. **84**, 4910 (2000).
18. Additional text and data are available on Science Online.

19. L. Petersen, P. Hofmann, E. W. Plummer, and F. Besenbacher, *J. Elect. Spec. Relat. Phen.* **109**, 97 (2000).
20. J. E. Hoffman *et al.*, *Science* **297**, 1148 (2002).
21. T. Ando, T. Nakanishi, and R. Saito, *J. Phys. Soc. Jpn.* **67**, 2857 (1998).
22. P. L. McEuen *et al.*, *Phys. Rev. Lett.* **83**, 5098 (1999).
23. We thank Mark Stiles, Emily Jarvis, Walt de Heer, XiaoSong Wu, Claire Berger, and F. Guinea for valuable comments and discussions, and Steven Blankenship, Frank Hess, Alan Band, and Nate Brown for their technical assistance. This work was supported in part by the Office of Naval Research, by Intel Research, and by NSF grant ECS-0404084.

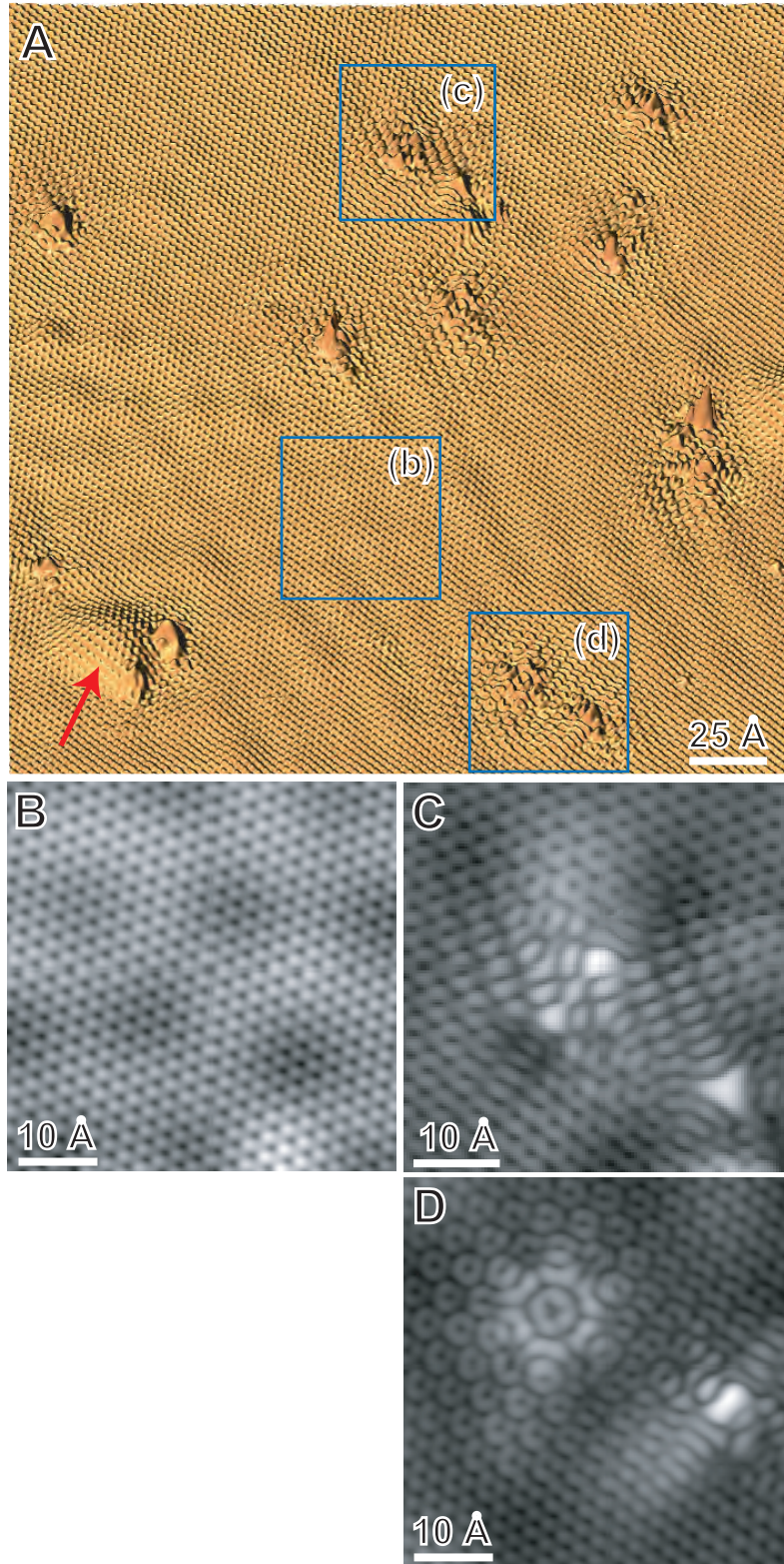


Figure 1, G. Rutter et. al.

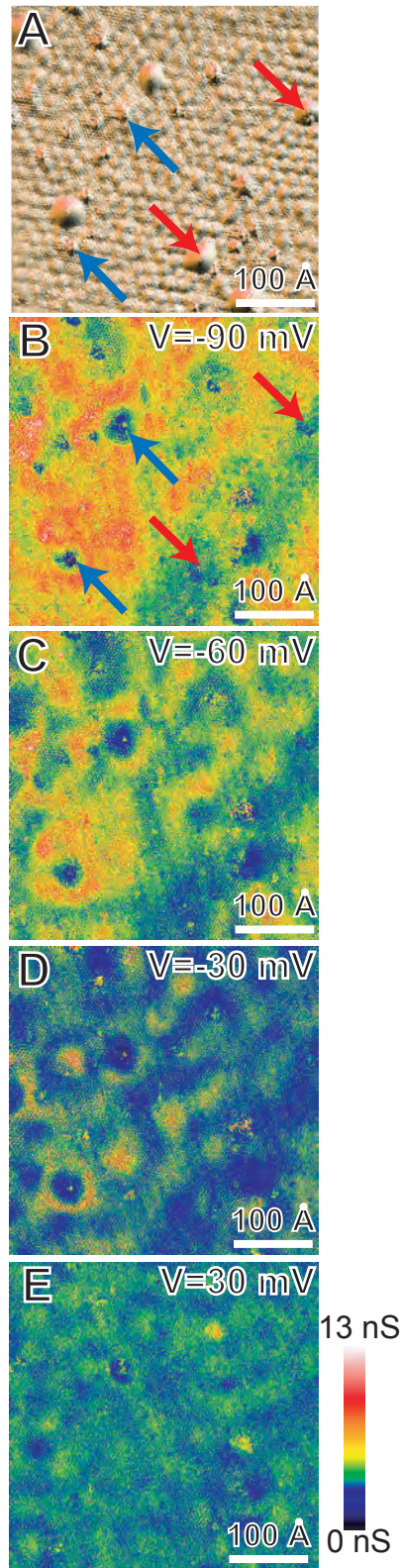


Figure 2, G. Rutter et. al.

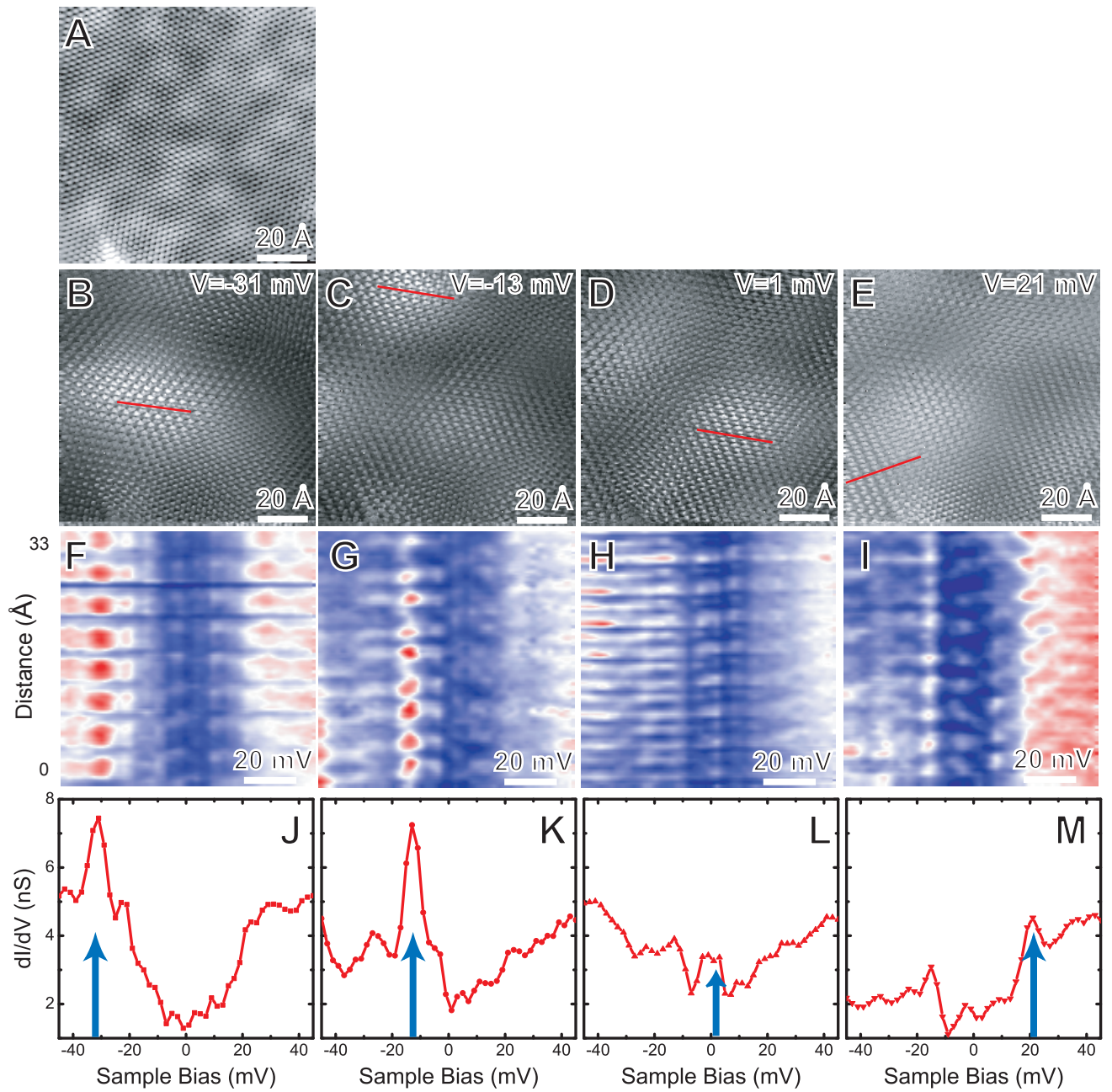


Figure 3, G. Rutter et. al.

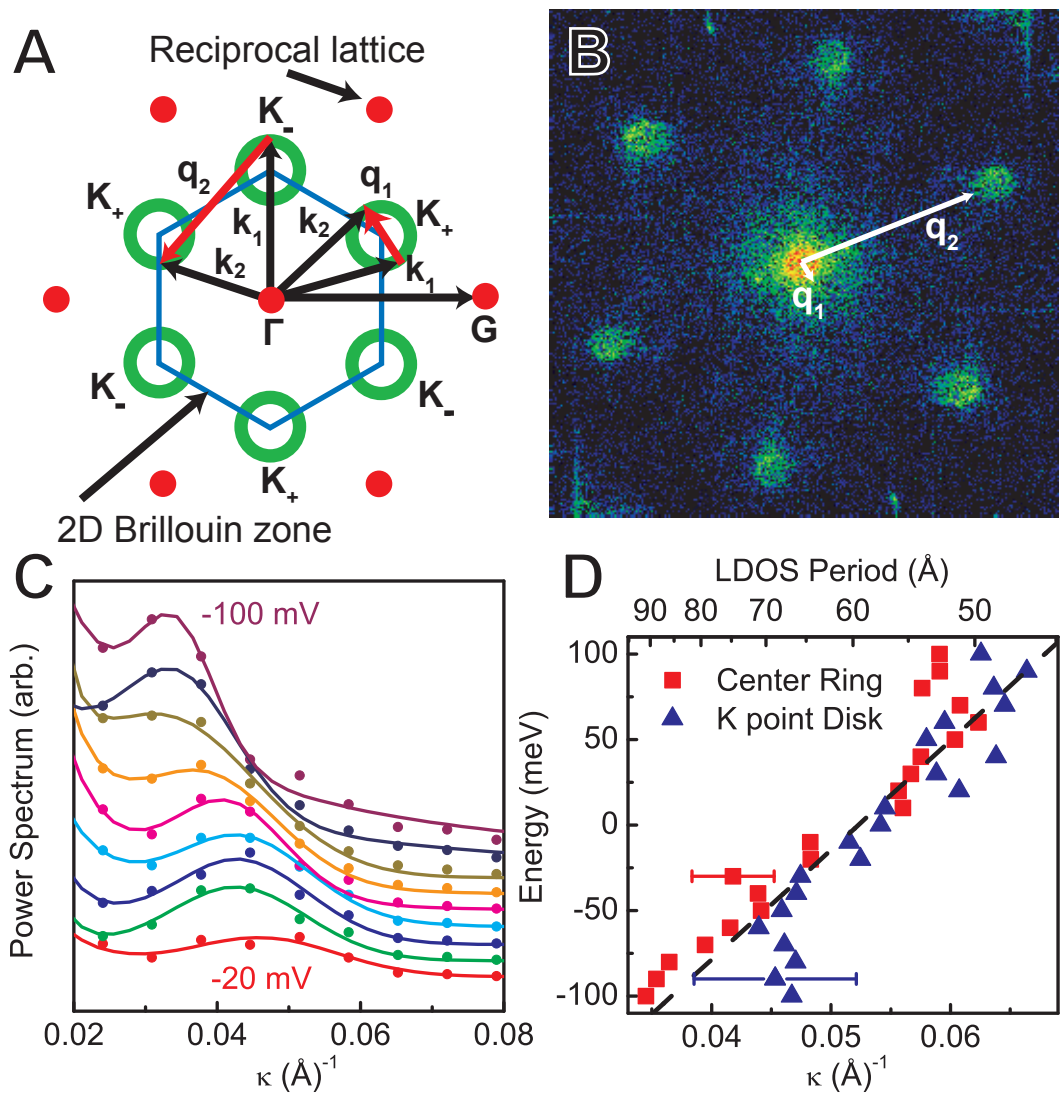


Figure 4, G. Rutter et. al.

Supporting Online Material for
Scattering and Interference in Epitaxial Graphene

G. M. Rutter, J. N. Crain, N. P. Guisinger, T. Li, P. N. First, J. A. Stroscio

This pdf file contains:

Material and methods, discussion of graphene symmetries and localization

Figs. S1 and S2

References

Symmetries of Graphene

Near the Fermi level, the quasiparticle band structure of graphene consists of upright and inverted cones that meet at a single energy E_D (the Dirac point), with this structure repeated at each of the six corners of the hexagonal Brillouin zone. Each corner of the Brillouin zone is equivalent (through a reciprocal lattice translation) to two of the others, leaving two inequivalent points, which we refer to as \mathbf{K}_+ and \mathbf{K}_- . As the Fermi level moves through E_D due to doping or an applied electric field, the Fermi surface becomes circular with radius κ centered at \mathbf{K}_\pm . Quasiparticle states near the Fermi-level in graphene can be described by the Dirac-like Hamiltonian, $H = \hbar v_f \boldsymbol{\sigma} \cdot \boldsymbol{\kappa}$, where $\boldsymbol{\sigma}$ is the 2D Pauli matrix used to describe the pseudospin property of the wavefunctions, and $\boldsymbol{\kappa} = \mathbf{k} - \mathbf{K}_\pm$ [1-3]. The pseudospin is a two-component vector that specifies the wavefunction amplitude on each of the two equivalent carbon sublattices, analogous to the two-component spinor describing electron spin. The wavefunctions contain an additional chiral symmetry for each Dirac cone at the two inequivalent corners of the Brillouin zone, \mathbf{K}_+ and \mathbf{K}_- . Chirality refers to the projection of $\boldsymbol{\sigma}$ on the direction of motion $\boldsymbol{\kappa}$. The chirality of electron states around \mathbf{K}_+ is right-handed (pseudospin parallel to $\boldsymbol{\kappa}$), whereas electron states around \mathbf{K}_- are left-handed (pseudospin antiparallel to $\boldsymbol{\kappa}$). For hole states, the sense of chirality is reversed. Many of the transport properties in graphene are affected by the conservation of chirality and pseudospin in long-wavelength scattering processes; in particular, for monolayer graphene backscattering is inhibited by these symmetries and can lead to anti-weak

localization [3,4]. Bilayer graphene has chiral properties similar to single-layer graphene [5]. Graphene quasiparticles may scatter and interfere due to the presence of short-range potentials from atomic-scale defects that locally break the symmetry of the Hamiltonian, and lead to a violation of the quasiparticle symmetry conservations. Such elastic scattering by short range potentials mixes electron states of the same energy, but different wavevectors \mathbf{k} , which may lie on the same constant energy contour (intravalley scattering) or on different contours of the same energy (intervalley scattering). In either case, the presence of a backscattering component results in a standing-wave pattern from the superposition of incident and scattered Bloch states, \mathbf{k}_1 and \mathbf{k}_2 . The wavevector of the standing wave is $\mathbf{q} = \mathbf{k}_2 - \mathbf{k}_1$ with wavelength, $\lambda = 2\pi / q$. This scattering wavelength is determined from the quasiparticle energy-momentum dispersion relation, $E(\mathbf{k})$. Thus, by mapping these scattering wave interference patterns, scanning tunneling spectroscopy (STS) provides a powerful tool to determine $E(\mathbf{k})$ on spatial scales comparable to the wavelengths of the standing-wave patterns [6-9].

Bilayer and Single Layer Graphene

The graphene bilayer can be distinguished from a single layer of graphene on SiC with STM measurements by simply counting the number of graphene layers from the substrate level; the latter can be determined with STS measurements [10]. The bilayer is characterized by a graphene lattice with a superimposed “6x6” modulation due to the underlying SiC reconstruction at the interface (see Fig. 1B). In contrast, the SiC reconstruction is much more apparent in the graphene monolayer, where adatom features can be seen “through” the graphene lattice (Fig. S1A) [10].

For a single graphene sheet, electronic states exhibit a linear band dispersion near the Fermi level, E_F (~ 300 meV above E_D for the studied samples), leading to zero effective mass. When a second sheet is added to form a bilayer, the states in the two layers may couple leading to two sets of bands [5,11,12]. A small gap at E_D is also expected because the two graphene layers are not identical due to the interface electric field. However, in the region describing the charge carriers near E_F , the dispersion for monolayer and bilayer are similar. It is near the Dirac (charge neutrality) point that the dispersions are different between the monolayer and the bilayer: linear for the monolayer and quadratic for the bilayer. Photoemission measurements find $E_F - E_D$ to be slightly smaller for the bilayer than for the monolayer [12].

Defect Scattering in Single Layer Graphene

Interference patterns from defect scattering are also visible in a single layer of epitaxial graphene (Fig. S1B). The Fermi level dI/dV map in Fig. S1B shows prominently the local $\sqrt{3} \times \sqrt{3}$ R30° structure due to \mathbf{q}_2 intervalley scattering. The black spots in the dI/dV map are due to SiC interface states beneath the graphene layer (Fig. S1A). The presence of long wavelength \mathbf{q}_1 scattering is less certain, partly due to the interface states. Further spectroscopic measurements with larger image sizes are needed to determine whether \mathbf{q}_1 -induced standing waves are completely absent for the monolayer. A preliminary measurement of the local dispersion for single layer graphene is thus only available from \mathbf{q}_2 scattering (Fig. S1, C and D). The monolayer dispersion follows the linear relation determined for the bilayer (Fig. S1D) with apparently a slightly more negative energy intercept, consistent with photoemission data [12].

Quasiparticle Localization and Transport

A phenomenological measure of the localization due to scattering in 2D systems can be obtained from the relative magnitude of the density of states corrugation [9]. Standing waves in two dimensions have zero LDOS at the nodes of the wavefunctions, therefore, localization in 2-dimensions yields large values for the relative LDOS corrugation, defined as $(dI/dV_{MEAN} - dI/dV_{MIN})/(dI/dV_{MEAN})$. Figure S2A shows histograms of the measured conductance values and the resulting corrugation amplitude as a function of energy, obtained from the data in Fig. 2. For energies near the Fermi-level, we find large values for the corrugation amplitude characteristic of localization in 2-dimensions [9]. Below E_F the corrugation remains relatively large, but for energies more than 30 meV above E_F , the corrugation amplitude decreases to below 40%. This is an indication of delocalization at higher energies, consistent with the diffuse features in the dI/dV map of Fig. 2E.

The identification of localized resonances that are tied to the interference maxima raises the question as to whether the observed states are related to weak localization, which is the self-interference of scattered waves along a connected path of random scatterers [13]. The energy-widths (~ 5 meV) of the dI/dV peaks in Fig. 3 imply a quasiparticle lifetime of $\tau_\phi \approx 0.1$ ps. The well-defined standing wave patterns indicate that the defects scatter elastically, so we estimate the elastic mean free path from the type B defect density ($n \approx 0.01$ nm⁻²) and $l_e \approx 1/(n\lambda_F) \approx 10$ nm, or $\tau_e = l_e/v_F = 10$ fs. In the diffusive limit, the coherence length (limited by inelastic scattering) is

$l_\varphi = \sqrt{(D\tau_\varphi)} \approx 25 \text{ nm}$, where $D = v_F^2 \tau_e / 2$ is the diffusion constant. This coherence length is somewhat smaller, but of the same order, as that obtained from the analysis of weak-localization in magnetotransport on a similar sample [14]. STS peaks very close to E_F , where peaks are seen with even smaller widths (approaching the temperature resolution limit), will have still larger coherence lengths.

Direct spectroscopic indications of weak localization in the tunneling spectra are 1) the substantially increased corrugation within $\pm 20 \text{ meV}$ of E_F (Fig. S2B), and 2) the reduced density of states near E_F that we observe in the conductance spectra (Fig. 3). It is clear from the scattering analysis that the band-structure density of states has no energy gap at E_F ; it increases monotonically. Therefore we believe that the persistent dip in the dI/dV spectra is a consequence of weak localization, for which a logarithmic suppression of the density of states at E_F is expected [15]. Still, a clear indication of weak localization requires further definitive measurements in a magnetic field to alter the phase coherence.

Reference List

1. T. Ando, T. Nakanishi, and R. Saito, J. Phys. Soc. Jpn. **67**, 2857 (1998).
2. P. L. McEuen *et al.*, Phys. Rev. Lett. **83**, 5098 (1999).
3. E. McCann *et al.*, Phys. Rev. Lett. **97**, 146805 (2006).
4. X. Wu *et al.*, Phys. Rev. Lett. **98**, 136801 (2007).
5. E. McCann and V. I. Fal'ko, Phys. Rev. Lett. **96**, 086805 (2006).

6. L. Petersen, P. Hofmann, E. W. Plummer, and F. Besenbacher, *J. Elec. Spec. Relat. Phen.* **109**, 97 (2000).
7. S. G. Lemay *et al.*, *Nature* **412**, 617 (2001).
8. J. E. Hoffman *et al.*, *Science* **297**, 1148 (2002).
9. M. Morgenstern *et al.*, *Phys. Rev. Lett.* **89**, 136806 (2002).
10. G. Rutter *et. al.* in preparation.
11. F. Guinea, A. H. C. Neto, and N. M. R. Peres, *Phys. Rev. B* **73**, 245426 (2006).
12. T. Ohta *et al.*, *Science* **313**, 951 (2006).
13. B. Kramer and A. Mackinnon, *Rep. Prog. Phys.* **56**, 1469 (1993).
14. C. Berger *et al.*, *J. Phys. Chem. B* **108**, 19912 (2004).
15. Y. Imry and Z. Ovadyahu, *Phys. Rev. Lett.* **49**, 841 (1982).

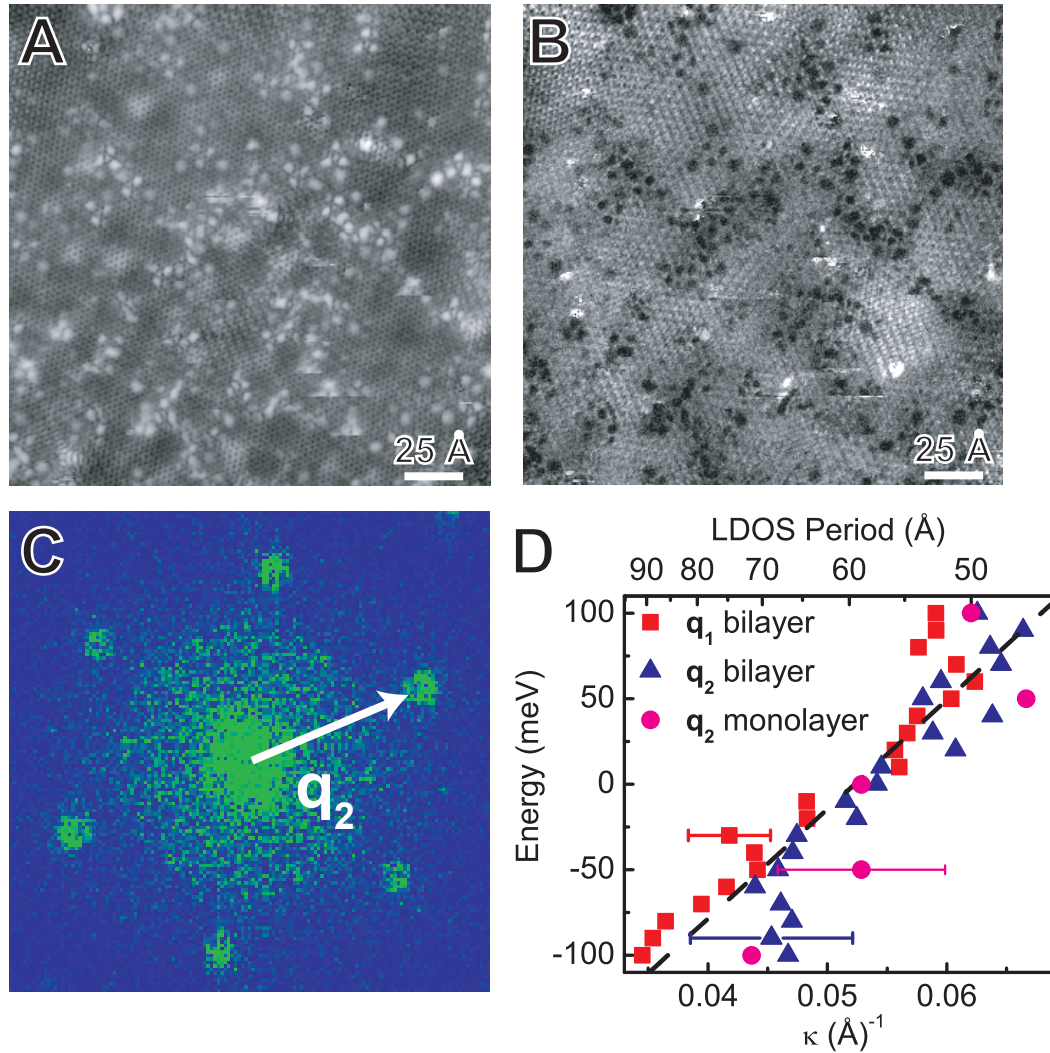


Figure S1: Scattering in single layer epitaxial graphene. (A) STM topographic image and (B) Simultaneously acquired dI/dV map at $V = 50$ mV. Tunneling setpoint: $I = 10$ pA, $V = -0.3$ V, $\Delta V = 10$ mV_{rms}. (C) \mathbf{q} -space map from the Fourier Transform power spectrum of the dI/dV map in (B) showing intervalley \mathbf{q}_2 scattering at the \mathbf{K}_\pm points. (D) Energy dispersion as a function of κ for single and bilayer layer graphene. Single layer values (magenta circles) are determined from the angle-averaged radii of the scattering disks at \mathbf{K}_\pm points as shown in (C), and are plotted with the bilayer values (red squares and blue triangles) from Fig. 4D. The dashed line is a linear fit to the bilayer data.

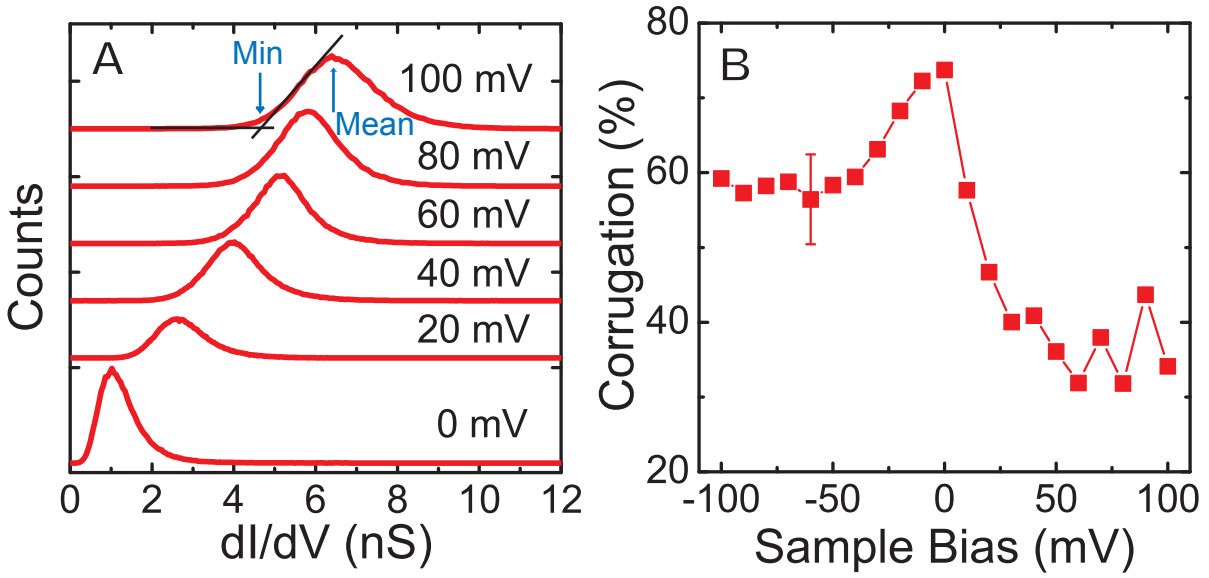


Figure S2: (A) Histograms of conductance values for the data set in Fig. 2 at selected values of the sample bias. The method for determining the minimum value of conductance is shown by the intersection of the two lines. Curves are offset for clarity. (B) Corresponding conductance corrugation $(dI/dV_{MEAN} - dI/dV_{MIN}) / (dI/dV_{MEAN})$ in the dI/dV maps as a function of sample bias.